One-pot synthesis of Ru/Nb$_2$O$_5$@Nb$_2$C ternary photocatalysts for water splitting by harnessing hydrothermal redox reactions

Wenkang Xu [a], Xiaoyao Li [a], Chao Peng [b], Guangxing Yang [a], Yonghai Cao [a], Hongjuan Wang [a], Feng Peng [c], Hao Yu [a,*]

[a] School of Chemistry and Chemical Engineering, Guangdong Provincial Key Lab of Green Chemical Product Technology, South China University of Technology, Guangzhou 510641, China
[b] School of Biotechnology and Health Sciences, Wuyi University, Jiangmen 529020, China
[c] School of Chemistry and Chemical Engineering, Guangzhou University, Guangzhou 510006, China

ARTICLE INFO

ABSTRACT

MXenes, 2D transition metal carbides/nitrides, have been demonstrated as promising platform for fabricating novel composites with interesting photo-/electrochemical properties. It is desirable to gain insights into the reactivity of MXenes, enabling the controllable transformation of MXenes. Here, a one-pot hydrothermal synthesis method of MXene-based photocatalyst is validated by harnessing the reducibility of Nb$_2$CT$_x$ MXene. The origin of reducibility of Nb$_2$CT$_x$ during the hydrothermal oxidation process was demonstrated as the active hydrogen produced from the water splitting in the presence of Nb$_2$CT$_x$, which reduced Ru^{3+} in situ to Ru nanoparticles on Nb$_2$O$_5$ nanowires derived from Nb$_2$CT$_x$. Compared with the traditional photo-deposition method, the chemical valance of the noble metal Ru/Pt obtained by the one-pot synthesis method was closer to the metal state, which reduced the charge transfer resistance by 82.5%. It led to the photocatalytic hydrogen production of 10.11 mmol·h^{-1}·g^{-1} with 41.25% apparent quantum yield at 313 nm.

1. Introduction

Solar hydrogen production is a sustainable approach to the supply of future energy with minimized risk to environment and high feasibility to be integrated into the existing chemical and energy industry via fuel cells and CO$_2$ utilization technology [1,2]. To this end, high performance semiconductor photocatalysts are highly desirable to overcome the recombination of excited carriers and the resulting low quantum yield [3]. Novel two-dimensional (2D) materials emerging since the discovery of graphene in 2004 have displayed the promise in fabricating photocatalysts with improved carrier transport and high quantum efficiency, such as graphene [4], transition metal dichalcogenides [5] and g-C$_3$N$_4$ [6].

Among them, MXenes, discovered in 2011 [7], have been regarded as an excellent platform to fabricate various photo-responsive composite materials [8] benefited from their hydrophilicity [9], photoelectric properties [10] and mobility of carriers [11]. Meanwhile, the 2D structure of MXene shortens the migration distance between carriers and the reaction interface, thereby weakens the recombination of carriers

[10], enabling MXenes as co-catalysts of photocatalytic hydrogen evolution reaction (HER) [12]. So far, it has been widely reported that MXene-containing hybrids can enhance the separation of photo-generated excitons, such as In$_2$S$_3$/TiO$_2$@Ti$_3$C$_2$T$_x$ [13], Cu$_2$O/(001) TiO$_2$@Ti$_3$C$_2$T$_x$ [14], etc. [15,16], implying that MXenes is promising as a photocatalytic HER co-catalyst.

Rich chemistry of MXene as 2D transition metal carbide is crucial to the synthesis strategy of MXene-based photocatalysts. It has been revealed that the work function of MXene is heavily dependent on the surface termination groups varying from 1.6 to 6 eV [17], which may tune the function of MXene as electronic or hole co-catalysts. For instance, the O-terminated Ti$_3$C$_2$ dots have been applied as co-catalysts of CdS to accept electrons and catalyze the production of hydrogen at high efficiency [11]. We demonstrated that the low work function of OH-terminated Ti$_3$C$_2$ MXenes enabled them as hole-trapper to reduce the recombination of carriers and elevate the hydrogen production [18]. Despite the surface chemistry, the chemical activity of carbides makes them as precursors to other compounds through redox reactions. In the partially oxidized MXenes, the oxide as the photocatalytic active site is

---

in close contact with MXenes, which is conducive to the transport of carriers [16]. The reducibility of MXenes has also been employed to directly reduce ions to generate metallic Pd, Au, Ag particles on MXene sheets without any additional reducing agents [19]. This self-reduction property suggests the promise of MXene in adsorptive removal of ionic pollutants, e.g. Cr(VI) [20], Pb(II) [21].

Here, a facile one-pot method is proposed to synthesize a ternary Ru/Nb_2O_5 @Nb_2C photocatalyst, in which Ru nanoparticles (NPs) act as sites for hydrogen production and Nb_2C sheets as co-catalyst separating carriers. By harnessing the hydrothermal reaction between Nb_2C MXene and water, it was achieved that the oxidative conversion of Nb_2C to semiconductor Nb_2O_5 nanowires [22] and the reductive deposition of Ru^{3+} occurred simultaneously to generate the ternary photocatalyst. It was demonstrated that the photocatalyst displayed high hydrogen production activity and quantum efficiency. The insight into the reducibility of MXene shows the superiority to the conventional post-photodepostion strategy of precious metal co-catalysts [23], due to the enhanced interfacial electron transfer.

2. Experimental

2.1. Synthesis of Nb_2C (MXene)

Nb_2C was prepared by the HF etching in the liquid phase [24]. In brief, 10 g Nb_2AlC (300 mesh, provided by Shenyang Institute of Metal Research, Chinese Academy of Sciences) were slowly added and dispersed into 100 mL of 49% HF (Aladdin, AR) in a Teflon reactor immersed in an oil bath at 60 °C. After 16 h, the muddy precipitate was washed with deionized water for five to six times until its pH was greater than 6.5. After vacuum drying and subsequent grinding, Nb_2C MXene powders were obtained.

2.2. Synthesis of Ru/Nb_2O_5@Nb_2C photocatalyst

150 mg Nb_2C was dispersed in 20 mL DI H_2O in a beaker. Then 1015 μL of 4 mg/mL $RuCl_3$ (Aladdin, 35.0–42.0% Ru) aqueous solution was added, being approximately equivalent to 1 wt% of Ru in the final catalyst. 95 mg $NaBF_4$ (Aladdin, AR, 99.0%) was then added as the crystal plane controlling agent of Nb_2O_5. The suspension was ultrasonically dispersed for 15 min, then transferred to a Teflon-lined autoclave. The autoclave was heated in an oven at 200 °C for 12 h. After the hydrothermal reaction, the solids were washed with deionized water and absolute ethanol successively and dried in vacuum overnight. The catalyst is denoted as RNN-*x-t-T*, in which *x* is the nominal loading of Ru (wt%), *t* is the hydrothermal duration (h), *T* is the temperature (°C) of the hydrothermal reaction. Table S1 lists the catalysts and synthesis conditions in this work. Similarly, PNN-1–12–200 (Pt/Nb_2O_5@Nb_2C) was prepared by the same method, except for replacing $RuCl_3$ with H_2PtCl_6.6 H_2O (Aladdin, AR, Pt≥37.5%).

A series of reference catalysts were prepared for comparative study. By replacing Nb_2C (MXene) with commercial NbC (Aladdin, 99%, 1–4 μm), RNN-C-1–12–200 photocatalyst was synthesized. To compare with post photo-deposition of Ru, Nb_2O_5@Nb_2C-12 h (NN–12–200) was firstly synthesized with the same procedure without adding $RuCl_3$ solution. 150 mg NN–12–200 were dispersed in 200 mL deionized water with 20 mL methanol. Then 1015 μL of the aforementioned $RuCl_3$ solution was added and sonicated for 15 min. Nitrogen was then injected continuously into the suspension in a beaker immersed in a water bath at 5 °C. The system was irradiated with 300 W Xenon lamp for 6 h. After the photodeposition reaction was completed, the solids were filtered, washed with deionized water and dried in vacuum overnight, denoted as NNR-*x-t-T* (Nb_2C@Nb_2O_5/Ru). To further compare the effect of support, Ru/Nb_2C was also prepared by directly impregnating $RuCl_3$ solution onto MXene Nb_2C [25]. By using commercial Nb_2O_5 (Aladdin, AR, 99.9%) rather than Nb_2O_5@Nb_2C-12 h as support, Ru/Nb_2O_5 catalyst was prepared with the same procedure as NNR-1–12–200. In order to

determine the transfer direction of photogenerated holes, 150 mg NN-4–200 were dispersed in 50 mL of 0.01 M $Pb(NO_3)_2$ solution. The pH was adjusted to 1 by adding nitric acid. The system was irradiated with 300 W Xenon lamp for 24 h. After the photodeposition was completed, the solids were filtered, washed with deionized water until pH > 6.5 and dried in vacuum overnight, denoted as PbO_2@NN-4–200.

2.3. Characterizations

The structure of catalyst was analyzed by an X-ray powder diffractometer (XRD, X'Pert3 Powder, PANalytical) using Cu-K_α radiation (λ_1 = 1.540598 Å ; λ_2 = 1.544426 Å, Ratio $K_{\alpha2}$/$K_{\alpha1}$=0.5) at a scan rate of 5° min^{-1}. The surface chemical state of the catalyst was analyzed by X-ray photoelectron spectroscopy (XPS, Karatos Axis Ultra DLD). The binding energy was corrected by contaminated carbon C 1 s at 284.8 eV. The surface morphology of the catalyst was observed by cold field-emission scanning electron microscopy (FE-SEM). The Brunauer-Emmett-Teller (BET) specific surface area (S_{BET}) of the catalyst was measured by N_2 absorption (TriStar II 3020). The microstructure was characterized by a JEM-2100 F transmission electron microscope operated at 200 kV. The composition was measured by an electronic probe analyzer (EPMA-1600). The UV-Vis diffuse reflectance spectroscopy of the catalysts was characterized by a UV-Vis spectrophotometer (DRS, U-3010). The photoluminescence (PL) spectra were measured on an F-7000 fluorescence spectrophotometer.

All the electrochemical tests were performed in a three-electrode electrochemical workstation (CHI660D) equipped with 300 W Xe lamp by using Ag/AgCl and a Pt net as the reference electrode and the counter electrode, respectively. The FTO glasses were used as the substrates to prepare the working electrodes: 4 mg sample powder and 20 μL 5% tetrafluoro sulfonic acid solution were dispersed in 180 μL absolute ethanol, and then sonicated for 15 min. Then, 40 μL dispersion was coated on a FTO glass with a size of 1 cm × 2.5 cm and dried at room temperature for 6 h. The transient photocurrent spectroscopy, the Mott-Schottky spectroscopy, and the electrochemical impedance spectroscopy were all tested with 0.1 M Na_2SO_4 aqueous solution as the electrolyte.

2.4. Photocatalytic experiments

The photocatalytic HERs and the apparent quantum efficiency (AQE) detection were conducted in a photocatalytic activity evaluation system (CEL-SPH2N, Aulight) equipped with a 300 W Xenon lamp (CEL-HXF300, Aulight). An online gas chromatograph was used for the detection of hydrogen content. The intensity of the light was measured by a full-spectrum strong light optical power meter (CEL-NP2000, Aulight, China). In a typical experiment, 10 mg as-prepared catalyst was dispersed in a glycerol solution (10 mL glycerol with 140 mL deionized water). The band-pass filter (Central wavelength: 313, 350, 365, 380, 420, 450, 500 nm, half-wave bandwidth was 20 nm) and UV reflector were used to achieve the monochromatic light for the AQE detection, and the effective spot radius was 3 cm.

3. Results and discussion

3.1. One-pot synthesis of Ru@Nb_2O_5/Nb_2C

It is widely documented that MXenes can be converted into corresponding oxides in the presence of oxidants, such as H_2O_2 [26], O_2 [27], CO_2 [16] and H_2O [18,28], because of the lower thermodynamical stability [29] and high oxyphilicity [30] of carbides. Under the hydrothermal conditions, the carbides extract oxygen from water and are converted into oxides, meanwhile CO_2 is released. This process can be facilely tuned by the addition of surfactants to manipulate the surface energy of oxides [31], thereby oxides with desirable morphology can be prepared. By this means, TiO_2 nanosheets with (0 0 1) facets exposed

[28] and [001] Nb_2O_5 nanorods [22] have been hybridized with MXenes for the photocatalytic hydrogen production [14,18,32] and CO_2 reduction [33]. It should be noted that the hydrothermal oxidation of MXenes produces hydrogen, as shown by the equation at the bottom of Fig. 1. The formation of hydrogen has been indicated by the hydrogen release from MXene prepared by HF etching [7], which may be originated from the hydrogen trapped between the layers [34]. Assuming that the hydrogen from water splitting can reduce metal ions, it is possible to convert MXene to semiconductor photocatalyst and decorate metal co-catalysts in single step. As illustrated in Fig. 1, a hierarchical ternary $Ru@Nb_2O_5/Nb_2C$ catalyst may be synthesized with the hydrothermal oxidation of Nb_2C MXene in Ru^{3+} aqueous solution, in which $NaBF_4$ can be used as surfactant to induce the growth of Nb_2O_5 along [001] direction [22].

Fig. 2(a) shows the XRD patterns of Nb_2AlC (MAX), Nb_2C (MXene), and RNN-1–12–200 by the one-pot synthesis method. After the HF etching, the reflections from Nb_2AlC disappeared, while the reflection of (002) planes of Nb_2C emerged at 7.5°, suggesting the formation of hexagonal Nb_2C MXenes [35].

The XRD pattern of RNN-1–12–200 shows two intense diffraction peaks from the reflections of (001) and (002) planes of orthorhombic Nb_2O_5. The absence of other reflections indicates the anisotropic growth of Nb_2O_5 in the presence of $NaBF_4$ as morphology modifier (see Fig. S1-S2). In addition, there was no any reflections from Ru species in the XRD pattern of RNN-1–12–200, suggesting the low content of Ru or the small crystallite size. The conversion of Nb_2C and growth of Nb_2O_5 can be further revealed by the evolution of XRD with reaction duration. As shown in Fig. S3, the RNN-1–6–200 sample exhibits stronger reflections from Nb_2C than that of RNN-1–12–200, indicating the gradual consumption of Nb_2C with the elongated reaction duration [36]. Meanwhile, the grain size of Nb_2O_5 (001) from the Sherrer equation expanded from 47.72 nm of RNN-1–6–200 to 59.38 nm of RNN-1–12–200, due to the growth of Nb_2O_5 along the [001] direction.

XPS was applied to identify the existence and chemical nature of Ru on RNN-1–12–200 photocatalyst. As shown in Fig. 2(b), the Ru3d core level XPS spectrum, overlapped with C1s, can be deconvoluted as a doublet at 280.5 and 284.4 eV for Ru $3d_{5/2}$ and Ru $3d_{3/2}$, respectively, which can be assigned as metallic Ru^0 [25,37], indicating that Ru^{3+} was reduced during the one-pot synthesis. The peak at 282.0 eV indicates the presence of Nb-C on Nb_2C [16].

Electron microscopy study was carried out to investigate the morphology and structure of the ternary photocatalyst. As shown by the SEM images in Fig. 3(a), after the one-pot hydrothermal synthesis, dense

nanowires with length of hundreds of nanometers cover the surface of accordion-like Nb_2C (Fig. S4) from etching Nb_2AlC by HF. The high-resolution SEM image in Fig. 3(b) clearly displays that the nanowires grow on the layered Nb_2C MXenes. The formation of nanowires significantly increased the specific surface area of RNN-1–12–200 (75.0 m^2/g) by 18.6 times of Nb_2C (Table S2), by which more active sites may be exposed for the photocatalytic reaction. Combining the XRD results, it can be expected that the nanowires are composed of Nb_2O_5 derived from Nb_2C.

TEM was employed to further identify the structure and composition of the nanowires. As shown in Fig. 3(c), the diameters of nanowires are in the range between 30 and 50 nm. HRTEM observation in Fig. 3(e) shows that the fringe spacing of the nanowire was 0.390 nm, corresponding to the (001) interplanar spacing of Nb_2O_5 (0.393 nm) (PDF#30–0873), verifying the growth of Nb_2O_5 nanowires. Meanwhile, the interlayer spacing of 0.91 nm from Nb_2C MXene was also identified in Fig. 3(d,e) [24,38].

Clusters of nanoparticles can be observed among the nanowires as highlighted in Fig. 3(f). The particle size statistics shows that the average diameter of Ru particles in Fig. 3(f) and extra TEM images in Fig. S5 is 2.6 ± 0.4 nm. The HRTEM shows the fringe intervals of 0.204 nm and 0.214 nm, which can be attributed to the (101) and (002) interplanar spacing of metallic Ru (PDF#06–0663). The HRTEM image in Fig. 3(g) shows a crystallite attached on the side of a Nb_2O_5 nanowire. The angle included by two sets of fringes of 63.0° is consistent with that of (002) and (101) planes of hexagonal ruthenium nanocrystal [39]. Furthermore, the EDS line scan analysis of a nanoparticle attached on the end of a Nb_2O_5 nanowire (Fig. 3 h) indicated that the particle is composed of Ru, while oxygen is insufficient in the particle, suggesting that the nanoparticle is a metallic Ru crystal rather than ruthenium oxide.

The generation of Ru NPs unambiguously demonstrated that there was reduction reaction of Ru^{3+} during the hydrothermal oxidation of Nb_2C. The scenario in Fig. 1 assumes that the reducing reagent is the active hydrogen from water splitting during the hydrothermal process. To verify this, a hydrogen trapping method was adopted using CCl_4 as the trapping reagent of hydrogen [40], which rapidly consumes active hydrogen atoms by the reaction:

$$CCl_4 + H \rightarrow *CCl_3 + H^+ + Cl^-.$$
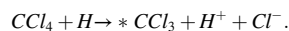
To do this, a certain amount of CCl_4 was added into the autoclave before the hydrothermal reaction. Assuming that 50% of Nb_2C was oxidized to Nb_2O_5 (see Table S3 for the estimation), 5.306 mmol H will be produced during the experiment through the hydrothermal reaction in Fig. 1. When 5.306 mmol (815 mg) CCl_4 was added, there was not any Ru detected in the final product, indicating that the reductive deposition of Ru^{3+} was completely quenched. Even only 0.53 mmol CCl_4 was added, the content of Ru in the final product significantly reduced from 1.00 to 0.47 wt% (see Table S1). The hydrogen capture reaction by CCl_4 can also be supported by the decline of pH of the reaction solution from 2.7 to 0.85 and 1.64 after the one-pot synthesis adding 5.306 and 0.53 mmol CCl_4, respectively, because of the generation of H^+. Above results demonstrate the activity of hydrogen produced by the hydrothermal reaction, which paves a new avenue to the simultaneous fabrication of MXene-hybridized photocatalyst with metal co-catalysts. Analogous to Ru, Pt co-catalysts can be deposited in the one-pot synthesis by replacing $RuCl_3$ with H_2PtCl_6 (see Fig. S6 and S7), demonstrating the generalization of this method.

3.2. Photocatalytic HER performance of $Ru@Nb_2O_5/Nb_2C$

The ternary RNN photocatalysts were subjected to the photocatalytic HER. Nb_2C MXene was completely inactive for HER, while the Nb_2O_5/Nb_2C hybrid (NN-12–200) reached a low hydrogen production rate of 0.42 mmol·g^{-1}·h^{-1} (Table S4). As shown in Fig. 4(a), the introduction of Ru significantly boosted the hydrogen production by 10–20 times. The highest hydrogen production, 10.11 mmol·g^{-1}·h^{-1} averaged for 5 h,
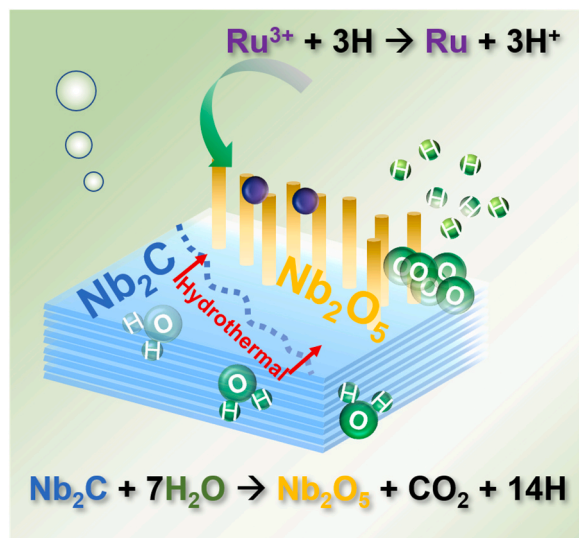

Fig. 1. Schematic diagram of the one-pot synthesis of $Ru@Nb_2O_5/Nb_2C$.
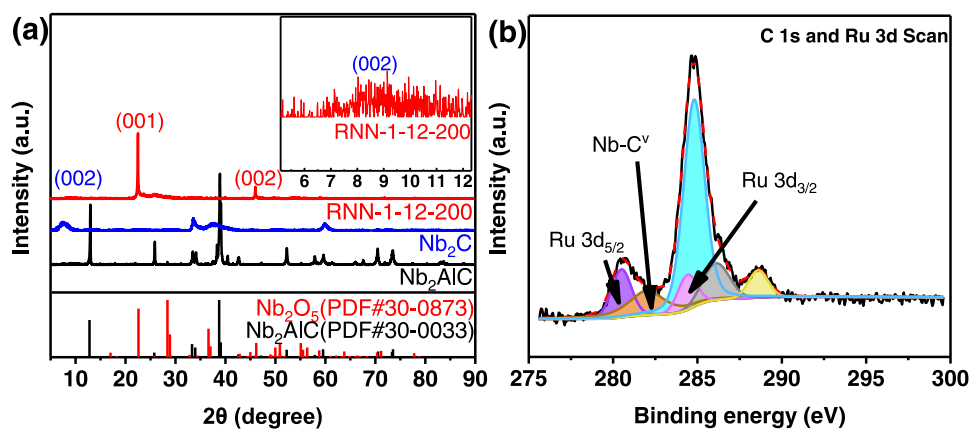
Fig. 2. (a) XRD patterns of Nb$_2$AlC (MAX), Nb$_2$C (MXene) and RNN-1–12–200 catalyst. The inset shows the (002) reflection of Nb$_2$C. (b) C 1 s/Ru 3d XPS spectrum of RNN-1–12–200 catalyst.
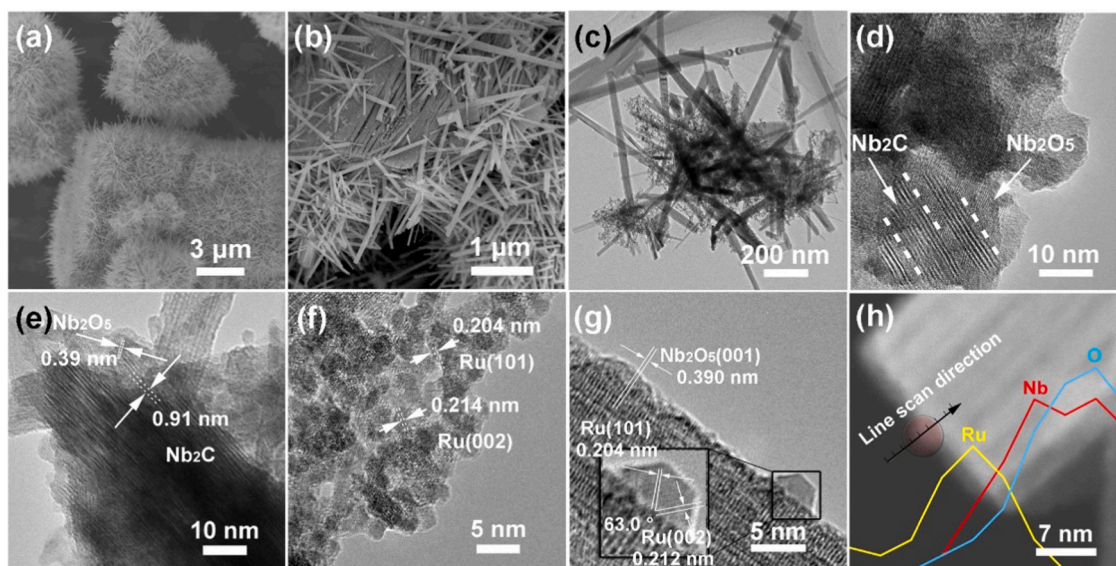

Fig. 3. (a, b) SEM images of RNN-1–12–200. (c-g) TEM images of RNN-1–12–200. (h) STEM-EDS line scan image of RNN-1–12–200.

was achieved with 1 wt% Ru nominal loading. Nb$_2$O$_5$ and Nb$_2$C are both indispensable for the photocatalysis, evidenced by the strong dependance of activity on the hydrothermal duration and temperature (Table S4), which determine the content of the semiconductor Nb$_2$O$_5$ and Nb$_2$C as co-catalyst [16,22]. In this work, the optimized hydrothermal reaction conditions were determined at 200 °C and 12 h, offering appropriate ratio of Nb$_2$C MXene and Nb$_2$O$_5$ semiconductor of about 1:1 molar ratio as determined in Table S3. Moreover, the RNN-1–12–200 remained 90% of the initial hydrogen after four consequent HER experiments, verifying the robustness of the photocatalyst (Fig. S8).

It should be noted that, with the optimized synthesis, the Ru@Nb$_2$O$_5$/Nb$_2$C ternary composite displayed the highest hydrogen production rate among the niobium based photocatalysts. Compared with our previous report using silver as co-catalyst of Nb$_2$O$_5$/Nb$_2$C [22], the adoption of Ru as co-catalyst and the unique one-pot synthesis resulted in significant improvement of activity by 15 folds. The Ru@Nb$_2$O$_5$/Nb$_2$C catalyst is also among the high activity photocatalysts derived from MXene materials, as shown in Table S5. Notably, the RNN-1–12–200 harvested an AQE of 41.25% at 313 nm (see Text S1 for calculation details of AQE), outperforming most of the MXene based photocatalysts. Fig. S9 shows the wavelength dependence of AQE of RNN-1–12–200. The AQE values declined to 3.43% at 350 nm, 0.704%

at 365 nm and 0.699% at 380 nm, respectively, and further to 0 at 420 nm and 450 nm, due to the obvious light absorption attenuation of Nb$_2$O$_5$ under visible light. This result implies that RNN-1–12–200 photocatalyst has a high utilization of light in the ultraviolet region (280–320 nm). Above results demonstrate the high efficiency of Ru@Nb$_2$O$_5$/Nb$_2$C ternary composite by the one-pot synthesis method as a wide-band-gap photocatalyst due to the forbidden gap of Nb$_2$O$_5$ of 3.1–4.0 eV [41,42].

The one-pot synthesis can be applied for the deposition of Pt co-catalyst either. As shown in Fig. 4(a), the PNN photocatalyst displays considerable hydrogen production of 6.14 mmol·g^{-1}·h^{-1}. The lower activity of PNN than that of RNN can be attributed to the larger size of Pt particles (see Fig. S6 and S7), which limits the amount of active sites for hydrogen production. It is interesting that the one-pot synthesis strategy shows distinct superiority to the traditional photo-deposition. As shown in Fig. 4(a), the NNR and NNP photocatalysts prepared by the photo-deposition of Ru and Pt, respectively, produced hydrogen with much lower reaction rates compared with the counterparts prepared by the one-pot synthesis in this work. The photocatalytic HER activity of the NNR catalyst was only 25% of that synthesized by the one-pot method, meanwhile the AQE of NNR drastically declined to 0.32% (Table S6). In addition, the photocatalytic HER performance of Pt@Nb$_2$O$_5$/Nb$_2$C was 1.38 times that of Nb$_2$C/Nb$_2$O$_5$ @Pt, associated with the decline of AQE
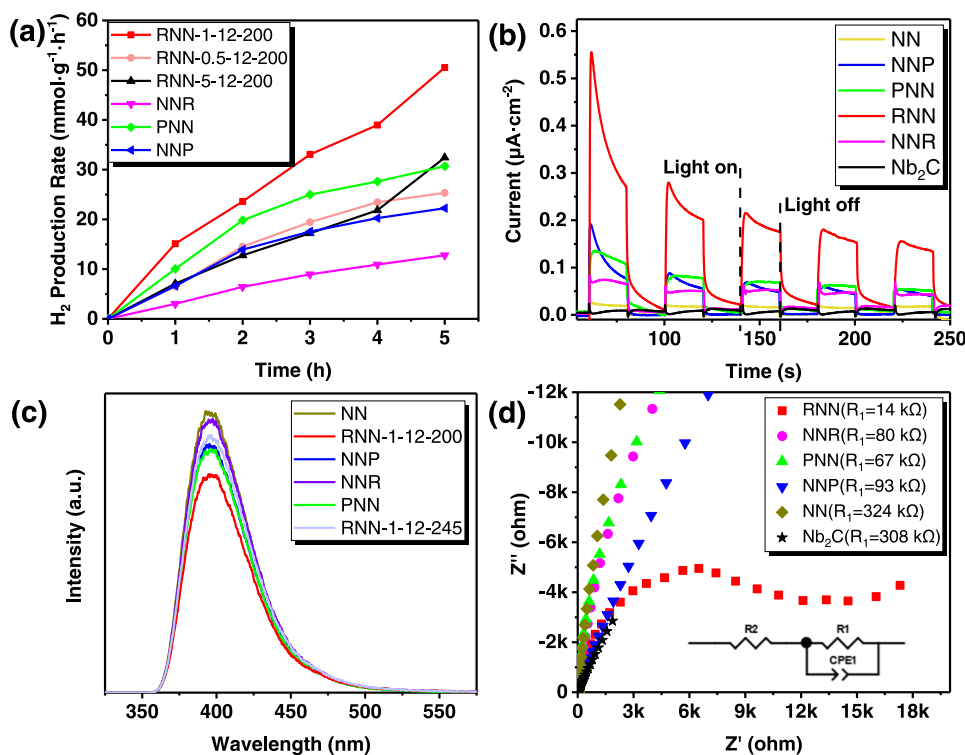
Fig. 4. (a) The hydrogen evolution on RNN photocatalysts with different Ru loading, NNR, PNN and NNP photocatalysts. (b) Transient photocurrent curves, (c) PL spectra and (d) Nyquist plots of the photocatalysts.

from 16.3% to 0.94%. The superiority was also revealed by transient photocurrent responses as shown in Fig. 4(b). Without Ru or Pt, the Nb_2O_5/Nb_2C hybrid displayed negligible photocurrent under irradiation. In the presence of Ru and Pt, the photocurrent was boosted in the

same rank as their HER activity: RNN>PNN>NNP>NNR.

The PL spectra shown in Fig. 4(c) indicates that the Nb_2O_5/Nb_2C hybrid and the Pt/Ru-loaded catalyst have similar PL signals, implying that the loading of Pt or Ru will not cause a new PL phenomenon. The
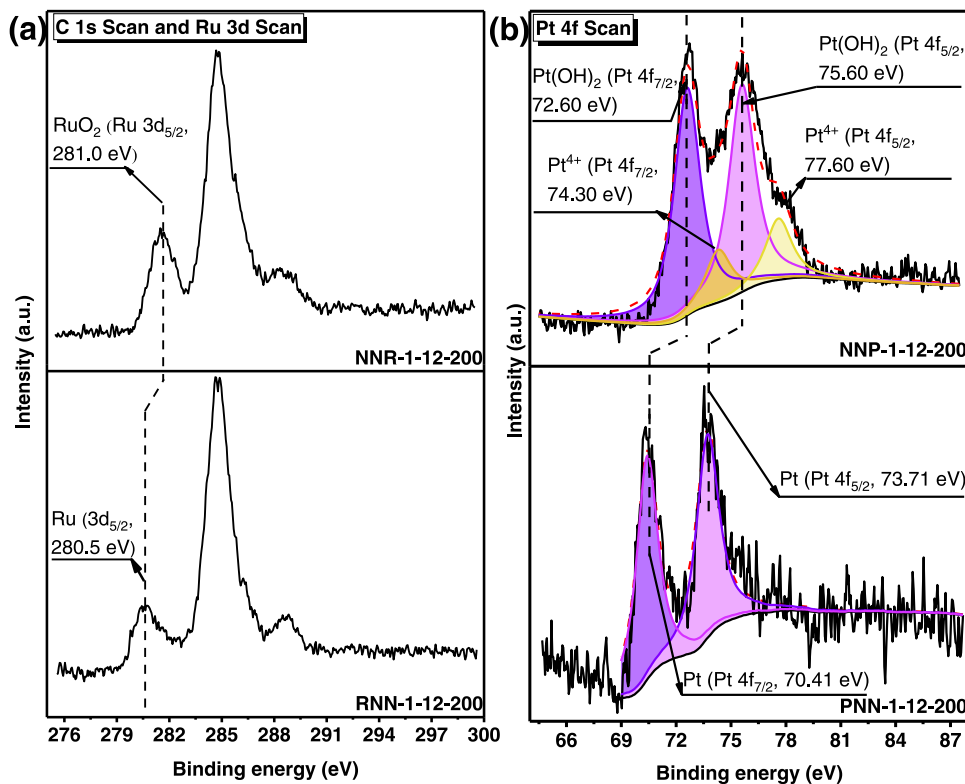

Fig. 5. (a) Ru 3d XPS spectra of RNN, NNR. (b) Pt 4f XPS spectra of PNN and NNP.

photocatalyst synthesized by the one-pot method had a weaker PL signal than those by the photo-deposition method, indicating that the lower recombination of electron-hole pairs of the photocatalyst is beneficial to the improvement of the photocatalytic performance [43]. According to the fluorescence intensity of RNN < PNN < NNP < NNR < NN, the presence of Pt/Ru effectively suppressed the recombination of photo-generated electrons and holes, thereby increasing the lifetime of photogenerated electrons.

To ascertain the charge transfer kinetics at the photoelectrode/ electrolyte interface, the electrochemical impedance spectroscopy (EIS) test was performed. As shown in Fig. 4(d), the Nyquist plot of RNN-1–12–200 has the smallest radius among the samples, indicating the enhanced transport efficiency of photogenerated electron-hole pairs represented by the equivalent resistance of 14 kΩ, which is less than one fifth of that of NNR photocatalyst and reduced the charge transfer resistance by 82.5%. Generally, the photocatalysts by the one pot synthesis exhibit smaller interfacial charge transfer resistance than those by traditional photo-deposition method, enabling the faster electron transfer and higher photocatalytic activity.

The significantly improved interfacial charge transfer can be rationalized by the well-developed metal-oxide interfaces formed by the highly active hydrogen atoms during the one pot synthesis. Fig. 5 compares the XPS spectra of metal co-catalysts (Ru or Pt) produced by the one pot synthesis and photo-deposition. Because the overlap of Ru3d and C1s region interfered the deconvolution, we did not fit the XPS spectra composed of Ru3d and C1s signal in Fig. 5(a). Nevertheless, the distinct shift of Ru 3d5/2 peak toward lower binding energy side by 0.5 eV was observed in RNN photocatalyst. It is indicative of the formation of metallic Ru species in RNN, while the Ru co-catalyst in NNR photocatalyst is mainly composed of Ru(III) or Ru(IV) [25]. This result was supported by the HRTEM image in Fig. S10. Similar results were obtained in the case of Pt as co-catalysts. As shown in Fig. 5(b), the Pt4f XPS spectrum of PNN photocatalyst displays sharp doublet peaks

centered at 70.41 and 73.71 eV, which are assigned as metallic Pt(0) [44]. However, only $Pt(OH)_2$ and Pt^{4+} species [45,46] were detected on NNP, suggesting that the photo-deposition cannot fully reduce the ionic state of Pt to the elemental metallic state [47]. The Pt species were further identified by HRTEM (Fig. S11). The interplanar spacings of 0.242 and 0.449 nm of NNP can be assigned as (311) and (−111) intervals of the monoclinic platinum hydrogen hydroxide $H_2Pt(OH)_6$, which are uniformly distributed on the Nb_2O_5 nanowire, with particle sizes of 2–3 nm. Thanks to the higher reducibility of active hydrogen species, the resultant Ru^0 or Pt^0 cocatalysts by the one-pot synthesis is superior in boosting photocatalytic performance and quantum yield because of the superior electronic conductivity [48], which significantly facilitates the electron transfer at the metal-oxide interfaces.

3.3. Photocatalytic mechanism of $Ru@Nb_2O_5/Nb_2C$

The energy band structure of $Ru@Nb_2O_5/Nb_2C$ was determined by Mott-Schottky (M-S) test and ultraviolet diffuse reflectance spectroscopy (DRUV-Vis), which allowed the further deduction of photocatalysis mechanism. As shown in Fig. 6(a), the black Nb_2C MXene has excellent light absorption in the range from 300 nm to 800 nm. The absorption significantly decreases after the hydrothermal reaction due to the consumption of Nb_2C, meanwhile the increase of absorbance in the 200–400 nm range is attributed to the formation of Nb_2O_5. Because the Nb_2C of RNN-1–12–245 has been almost completely converted to Nb_2O_5 during the synthesis process (Table S3), the light absorption behavior of RNN-1–12–245 is close to that of commercial Nb_2O_5. The bandgap widths of the Nb_2O_5 photocatalysts were determined by the Tauc curves (Fig. 6b) as 3.09 eV, while the bandgap widths of the photocatalysts synthesized at 200 °C are 3.25 eV regardless of the type of cocatalysts and synthesis method. The E_{CB} and flat band potential (E_{FB}) were determined by the M-S curves. Fig. 6(c) shows that the slopes of M-S curves are positive, because Nb_2O_5 is an *n*-type semiconductor. The M-S
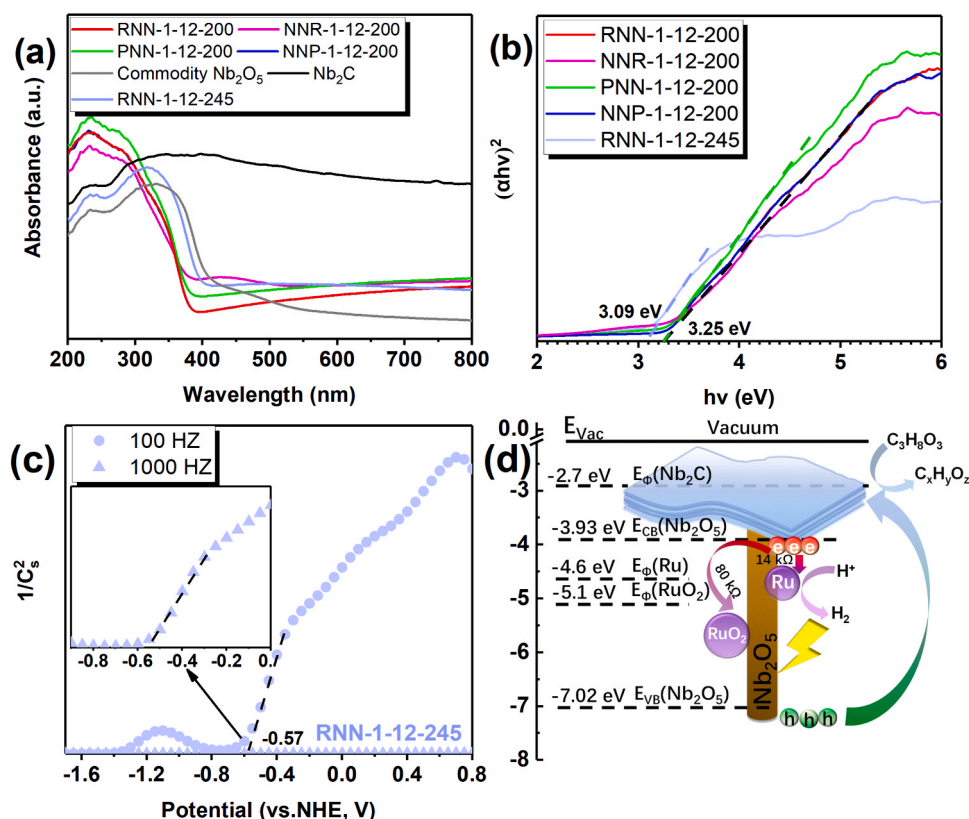

Fig. 6. (a) DRUV-Vis spectra and (b) Tauc's plots of various photocatalysts. (c) Mott-Schottky curves of RNN-1–12–245. (d) Energy band structure of RNN-1–12–200.

curves of RNN-1–12–245 at 100 Hz, and 1000 Hz intersect at -0.57 V (vs. NHE). For *n*-type semiconductors, the gap between the flat charge potential and the minimum of E_{CB} can be ignored, thus the minimum of E_{CB} can be determined as -0.57 V (vs. NHE). Converting the standard hydrogen potential (E(V)) into a vacuum level (E (eV)), the E_{CB} of Nb_2O_5 can be determined as -3.93 eV, which is consistent with our previous report [22]. The valence band energy E_{VB} is thus calculated at 7.02 eV from E_{CB} minus bandgap width, which is also close to our previous report value of 7.05 eV [22].

The photocatalytic mechanism can be rationalized as Fig. 6(d). In our previous research, Nb_2C plays as a hole-conducting medium in the MXene-based photocatalyst because of the low work function of OH-terminated Nb_2C, 2.7 eV [8,22]. The photodeposition of PbO_2 was carried out to determine the transfer direction of photogenerated holes. To this end, NN-4–200 sample was selected as the substrate, on which the short hydrothermal time guaranteed the exposure of Nb_2C nanosheet from the dense coverage of Nb_2O_5 nanowires as shown in Fig. 3(a). As shown in Fig. S12 (a, b), PbO_2 nanoparticles can be identified. In the heterojunction structure, PbO_2 particles are mainly deposited on the layered Nb_2C, while not found on Nb_2O_5. This can be confirmed by STEM-EDS mapping (see Fig. S12 c, d), manifesting that Nb_2C serves as photocatalytic oxidation sites where PbO_2 particles are photodeposited because of the oxidation by photogenerated holes.[49] It indicates that photogenerated holes transfer from Nb_2O_5 to Nb_2C under irradiation. On the other hand, the electron transfer was supported by the photo-deposition of Pt. As shown in Fig. S11 (a, c, d), the photodeposition of platinum occurred on Nb_2O_5 nanowires, while is absent on the layered Nb_2C (Fig. S11 b). It suggests that the reduction sites are mainly on Nb_2O_5 nanowires instead of Nb_2C.

Ru has a work function of 4.6 eV [50], acting as an electron trap. The excellent electron transfer between Ru and Nb_2O_5 enhances the separation of photogenerated carriers in RNN catalyst. Obviously, the incomplete reduction of precious metal ions will increase the work function of co-catalyst and the interfacial resistance, thus deteriorate the electron transfer. In our study, it is highlighted that the well-designed synthesis may drastically improve the interfacial electron transfer of the MXene based ternary photocatalyst, by harnessing the active hydrogen in situ produced during the hydrothermal oxidation of MXenes.

4. Conclusion

A hierarchical Ru/Nb_2O_5@Nb_2C photocatalyst was synthesized by a one-pot hydrothermal method, which provided a more complete reduction for depositing metallic co-catalysts on MXene-based photocatalysts. It was demonstrated that Ru(III) or Pt(IV) can be reduced to Ru^0 or Pt^0 in situ by the active H produced from the hydrothermal oxidation of Nb_2C MXene without additional reducing agent. The optimum synthesis procedures allowed for the significantly enhanced photocatalytic hydrogen production at 10.11 mmol g^{-1} h^{-1} and AQE of 41.25% at 313 nm. Compared with the common photo-deposition method, the one-pot hydrothermal method not only has the advantage of simple steps, but also forms well-developed metal/semiconductor/MXene heterojunction to reduce the photo-generated carrier transfer resistance and harvests better photocatalytic HER performance. This insight into the reactivity of MXenes for oxidation and reduction reactions provides a universal new approach to the facile synthesis of MXene-based photocatalysts.

CRediT authorship contribution statement

Wenkang Xu: Investigation, Writing – original draft. **Xiaoyao Li:** Investigation. **Chao Peng:** Review. **Guangxing Yang:** Review and editing. **Yonghai Cao:** Review. **Hongjuan Wang:** Review. **Feng Peng:** Review. **Hao Yu:** Conceptualization, Supervision, Funding acquisition, Review and editing.

Declaration of Competing Interest

The authors declare that they have no known competing financial interests or personal relationships that could have appeared to influence the work reported in this paper.

Acknowledgement

Appendix A. Supporting information

Supplementary data associated with this article can be found in the online version at doi:10.1016/j.apcatb.2021.120910.

References

[1] C. Liu, B.C. Colon, M. Ziesack, P.A. Silver, D.G. Nocera, Water splitting-biosynthetic system with CO_2 reduction efficiencies exceeding photosynthesis, Science 352 (2016) 1210–1213, https://doi.org/10.1126/science.aaf5039.

[2] C. Wei, R.R. Rao, J. Peng, B. Huang, I.E.L. Stephens, M. Risch, Z.J. Xu, Y. Shao-Horn, Recommended practices and benchmark activity for hydrogen and oxygen electrocatalysis in water splitting and fuel cells, Adv. Mater. 31 (2019), 1806296, https://doi.org/10.1002/adma.201806296.

[3] D. Ma, J. Li, A. Liu, C. Chen, Carbon gels-modified TiO_2: promising materials for photocatalysis applications, Materials 13 (2020) 1734, https://doi.org/10.3390/ma13071734.

[4] N. Zhang, M.-Q. Yang, S. Liu, Y. Sun, Y.-J. Xu, Waltzing with the versatile platform of graphene to synthesize composite photocatalysts, Chem. Rev. 115 (2015) 10307–10377, https://doi.org/10.1021/acs.chemrev.5b00267.

[5] Z. Liang, R. Shen, Y.H. Ng, P. Zhang, Q. Xiang, X. Li, A review on 2D MoS_2 cocatalysts in photocatalytic H_2 production, J. Mater. Sci. Technol. 56 (2020) 89–121, https://doi.org/10.1016/j.jmst.2020.04.032.

[6] Y.-J. Yuan, Z. Shen, S. Wu, Y. Su, L. Pei, Z. Ji, M. Ding, W. Bai, Y. Chen, Z.-T. Yu, Z. Zou, Liquid exfoliation of g-C_3N_4 nanosheets to construct 2D–2D MoS_2/g-C_3N_4 photocatalyst for enhanced photocatalytic H_2 production activity, Appl. Catal. B-Environ. 246 (2019) 120–128, https://doi.org/10.1016/j.apcatb.2019.01.043.

[7] M. Naguib, M. Kurtoglu, V. Presser, J. Lu, J. Niu, M. Heon, L. Hultman, Y. Gogotsi, M.W. Barsoum, Two-dimensional nanocrystals produced by exfoliation of Ti_3AlC_2, Adv. Mater. 23 (2011) 4248–4253, https://doi.org/10.1002/adma.201102306.

[8] C. Peng, T. Zhou, P. Wei, W. Xu, H. Pan, F. Peng, J. Jia, K. Zhang, H. Yu, Photocatalysis over MXene-based hybrids: Synthesis, surface chemistry, and interfacial charge kinetics, APL Mater. 9 (2021), 070703, https://doi.org/10.1063/5.0055711.

[9] Z. Ling, C.E. Ren, M.-Q. Zhao, J. Yang, J.M. Giammarco, J. Qiu, M.W. Barsoum, Y. Gogotsi, Flexible and conductive MXene films and nanocomposites with high capacitance, Proc. Natl. Acad. Sci. U. S. A. 111 (2014) 16676–16681, https://doi.org/10.1073/pnas.1414215111.

[10] Q. Zhong, Q. Li, G. Zhang, Two-dimensional MXene-based and MXene-derived photocatalysts: Recent developments and perspectives, Chem. Eng. J. 409 (2020), 128099, https://doi.org/10.1016/j.cej.2020.128099.

[11] J. Ran, G. Gao, F.-T. Li, T.-Y. Ma, A. Du, S.-Z. Qiao, Ti_3C_2 MXene co-catalyst on metal sulfide photo-absorbers for enhanced visible-light photocatalytic hydrogen production, Nat. Commun. 8 (2017) 13907, https://doi.org/10.1038/ncomms13907.

[12] L. Cheng, X. Li, H. Zhang, Q. Xiang, Two-dimensional transition metal mxene-based photocatalysts for solar fuel generation, J. Phys. Chem. Lett. 10 (2019) 3488–3494, https://doi.org/10.1021/acs.jpclett.9b00736.

[13] H. Wang, Y. Wu, T. Xiao, X. Yuan, G. Zeng, W. Tu, S. Wu, H.Y. Lee, Y.Z. Tan, J. W. Chew, Formation of quasi-core-shell In_2S_3/anatase TiO_2@metallic $Ti_3C_2T_x$ hybrids with favorable charge transfer channels for excellent visible-light-photocatalytic performance, Appl. Catal. B-Environ. 233 (2018) 213–225, https://doi.org/10.1016/j.apcatb.2018.04.012.

[14] C. Peng, W. Xu, P. Wei, M. Liu, L. Guo, P. Wu, K. Zhang, Y. Cao, H. Wang, H. Yu, F. Peng, X. Yan, Manipulating photocatalytic pathway and activity of ternary Cu_2O/(001)TiO_2@$Ti_3C_2T_x$ catalysts for H_2 evolution: Effect of surface coverage, Int. J. Hydrog. Energy 44 (2019) 29975–29985, https://doi.org/10.1016/j.ijhydene.2019.09.190.

[15] Y. Li, L. Ding, Z. Liang, Y. Xue, H. Cui, J. Tian, Synergetic effect of defects rich MoS_2 and Ti_3C_2 MXene as cocatalysts for enhanced photocatalytic H_2 production activity of TiO_2, Chem. Eng. J. 383 (2020), 123178, https://doi.org/10.1016/j.cej.2019.123178.

[16] T. Su, R. Peng, Z.D. Hood, M. Naguib, I.N. Ivanov, J.K. Keum, Z. Qin, Z. Guo, Z. Wu, One-Step Synthesis of Nb_2O_5/C/Nb_2C (MXene) Composites and Their Use as Photocatalysts for Hydrogen Evolution, ChemSusChem 11 (2018) 688–699, https://doi.org/10.1002/cssc.201702317.

[17] M. Khazaei, M. Arai, T. Sasaki, A. Ranjbar, Y. Liang, S. Yunoki, OH-terminated two-dimensional transition metal carbides and nitrides as ultralow work function

materials, Phys. Rev. B. 92 (2015), 075411, https://doi.org/10.1103/PhysRevB.92.075411.

[18] C. Peng, P. Wei, X. Li, Y. Liu, Y. Cao, H. Wang, H. Yu, F. Peng, L. Zhang, B. Zhang, K. Lv, High efficiency photocatalytic hydrogen production over ternary Cu/TiO₂@Ti₃C₂Tₓ enabled by low-work-function 2D titanium carbide, Nano Energy 53 (2018) 97–107, https://doi.org/10.1016/j.nanoen.2018.08.040.

[19] E. Satheeshkumar, T. Makaryan, A. Melikyan, H. Minassian, Y. Gogotsi, M. Yoshimura, One-step solution processing of Ag, Au and Pd@MXene hybrids for SERS, Sci. Rep. 6 (2016) 32049, https://doi.org/10.1038/srep32049.

[20] Y. Ying, Y. Liu, X. Wang, Y. Mao, W. Cao, P. Hu, X. Peng, Two-dimensional titanium carbide for efficiently reductive removal of highly toxic chromium(vi) from water, ACS Appl. Mater. Interfaces 7 (2015) 1795–1803, https://doi.org/10.1021/am5074722.

[21] Q. Peng, J. Guo, Q. Zhang, J. Xiang, B. Liu, A. Zhou, R. Liu, Y. Tian, Unique lead adsorption behavior of activated hydroxyl group in two-dimensional titanium carbide, J. Am. Chem. Soc. 136 (2014) 4113–4116, https://doi.org/10.1021/ja500506k.

[22] C. Peng, X. Xie, W. Xu, T. Zhou, P. Wei, J. Jia, K. Zhang, Y. Cao, H. Wang, F. Peng, R. Yang, X. Yan, H. Pan, H. Yu, Engineering highly active Ag/Nb₂O₅@Nb₂CTₓ (MXene) photocatalysts via steering charge kinetics strategy, Chem. Eng. J. 421 (2021), 128766, https://doi.org/10.1016/j.cej.2021.128766.

[23] H. Wang, Y. Sun, Y. Wu, W. Tu, S. Wu, X. Yuan, G. Zeng, Z.J. Xu, S. Li, J.W. Chew, Electrical promotion of spatially photoinduced charge separation via interfacial-built-in quasi-alloying effect in hierarchical Zn₂In₂S₅/Ti₃C₂(O, OH)ₓ hybrids toward efficient photocatalytic hydrogen evolution and environmental remediation, Appl. Catal. B-Environ. 51 (2018) 206–213, https://doi.org/10.1016/j.apcatb.2018.12.051.

[24] M. Naguib, J. Halim, J. Lu, K.M. Cook, L. Hultman, Y. Gogotsi, M.W. Barsoum, New two-dimensional niobium and vanadium carbides as promising materials for Li-Ion batteries, J. Am. Chem. Soc. 135 (2013) 15966–15969, https://doi.org/10.1021/ja405735d.

[25] Y. Liu, Y.-H. Li, X. Li, Q. Zhang, H. Yu, X. Peng, F. Peng, Regulating electron–hole separation to promote photocatalytic h2 evolution activity of nanoconfined Ru/MXene/TiO₂ catalysts, ACS Nano 14 (2020) 14181–14189, https://doi.org/10.1021/acsnano.0c07089.

[26] Y. Dong, Z.-S. Wu, S. Zheng, X. Wang, J. Qin, S. Wang, X. Shi, X. Bao, Ti₃C₂ MXene-derived sodium/potassium titanate nanoribbons for high-performance sodium/potassium ion batteries with enhanced capacities, ACS Nano 11 (2017) 4792–4800, https://doi.org/10.1021/acsnano.7b01165.

[27] A. Lipatov, M. Alhabeb, M.R. Lukatskaya, A. Boson, Y. Gogotsi, A. Sinitskii, Effect of synthesis on quality, electronic properties and environmental stability of individual monolayer Ti₃C₂ MXene Flakes, Adv. Electron. Mater. 2 (2016), 1600255, https://doi.org/10.1002/aelm.201600255.

[28] C. Peng, X. Yang, Y. Li, H. Yu, H. Wang, F. Peng, Hybrids of two-dimensional Ti₃C₂ and TiO₂ exposing {001} facets toward enhanced photocatalytic activity, ACS Appl. Mater. Interfaces 8 (2016) 6051–6060, https://doi.org/10.1021/acsami.5b11973.

[29] T. Habib, X. Zhao, S.A. Shah, Y. Chen, W. Sun, H. An, J.L. Lutkenhaus, M. Radovic, M.J. Green, Oxidation stability of Ti₃C₂Tₓ MXene nanosheets in solvents and composite films, npj 2D Mater. Appl. 3 (2019) 8, https://doi.org/10.1038/s41699-019-0089-3.

[30] M. Ashton, K. Mathew, R.G. Hennig, S.B. Sinnott, Predicted surface composition and thermodynamic stability of MXenes in solution, J. Phys. Chem. C. 120 (2016) 3550–3556, https://doi.org/10.1021/acs.jpcc.5b11887.

[31] M.S. Bakshi, How surfactants control crystal growth of nanomaterials, Cryst. Growth Des. 16 (2016) 1104–1133, https://doi.org/10.1021/acs.cgd.5b01465.

[32] Y. Li, Z. Yin, G. Ji, Z. Liang, Y. Xue, Y. Guo, J. Tian, X. Wang, H. Cui, 2D/2D/2D heterojunction of Ti₃C₂ MXene/MoS₂ nanosheets/TiO₂ nanosheets with exposed (001) facets toward enhanced photocatalytic hydrogen production activity, Appl. Catal. B-Environ. 246 (2019) 12–20, https://doi.org/10.1016/j.apcatb.2019.01.051.

[33] L. Chen, K. Huang, Q. Xie, S.M. Lam, J.C. Sin, T. Su, H. Ji, Z. Qin, The enhancement of photocatalytic CO₂ reduction by the in situ growth of TiO₂ on Ti₃C₂ MXene, Catal. Sci. Technol. 11 (2021) 1602–1614, https://doi.org/10.1039/D0CY02212H.

[34] N.C. Osti, M. Naguib, M. Tyagi, Y. Gogotsi, A.I. Kolesnikov, E. Mamontov, Evidence of molecular hydrogen trapped in two-dimensional layered titanium carbide-based

[35] H. Lin, S. Gao, C. Dai, Y. Chen, J. Shi, A two-dimensional biodegradable niobium carbide (mxene) for photothermal tumor eradication in NIR-I and NIR-II biowindows, J. Am. Chem. Soc. 139 (2017) 16235–16247, https://doi.org/10.1021/jacs.7b07818.

[36] D. Zu, H. Song, Y. Wang, Z. Chao, Z. Li, G. Wang, Y. Shen, C. Li, J. Ma, One-pot in-situ hydrothermal synthesis of CdS/Nb₂O₅/Nb₂C heterojunction for enhanced visible-light-driven photodegradation, Appl. Catal. B-Environ. 277 (2020), 119140, https://doi.org/10.1016/j.apcatb.2020.119140.

[37] J.Y. Shen, A. Adnot, S. Kaliaguine, An ESCA study of the interaction of oxygen with the surface of ruthenium, Appl. Surf. Sci. 51 (1991) 47–60, https://doi.org/10.1016/0169-4332(91)90061-N.

[38] C. Zhang, M. Beidaghi, M. Naguib, M.R. Lukatskaya, M.-Q. Zhao, B. Dyatkin, K. M. Cook, S.J. Kim, B. Eng, X. Xiao, D. Long, W. Qiao, B. Dunn, Y. Gogotsi, Synthesis and charge storage properties of hierarchical niobium pentoxide/carbon/niobium carbide (MXene) hybrid materials, Chem. Mat. 28 (2016) 3937–3943, https://doi.org/10.1021/acs.chemmater.6b01244.

[39] H. Ye, Q. Wang, M. Catalano, N. Lu, J. Vermeylen, M.J. Kim, Y. Liu, Y. Sun, X. Xia, Ru nanoframes with an fcc structure and enhanced catalytic properties, Nano Lett. 16 (2016) 2812–2817, https://doi.org/10.1021/acs.nanolett.6b00607.

[40] H. Robert, P. Schuler, Neta, Richard, W. Fessenden, Electron spin resonance study of the rate constants for reaction of hydrogen atoms with organic compounds in aqueous solution, J. Phys. Chem. 75 (1971) 1654–1666, https://doi.org/10.1021/j100906a004.

[41] A.G.S. Prado, L.B. Bolzon, C.P. Pedroso, A.O. Moura, L.L. Costa, Nb₂O₅ as efficient and recyclable photocatalyst for indigo carmine degradation, Appl. Catal. B-Environ. 82 (2008) 219–224, https://doi.org/10.1016/j.apcatb.2008.01.024.

[42] M.A. de Araújo, M.F. Gromboni, F. Marken, S.C. Parker, L.M. Peter, J. Turner, H. C. Aspinall, K. Black, L.H. Mascaro, Contrasting transient photocurrent characteristics for thin films of vacuum-doped "grey" TiO₂ and "grey" Nb₂O₅, Appl. Catal. B-Environ. 237 (2018) 339–352, https://doi.org/10.1016/j.apcatb.2018.05.065.

[43] Y. Bu, Z. Chen, C. Sun, Highly efficient Z-Scheme Ag₃PO₄/Ag/WO₃₋ₓ photocatalyst for its enhanced photocatalytic performance, Appl. Catal. B-Environ. 179 (2015) 363–371, https://doi.org/10.1016/j.apcatb.2015.05.045.

[44] A.M. Motin, T. Haunold, A.V. Bukhtiyarov, A. Bera, C. Rameshan, G. Rupprechter, Surface science approach to Pt/carbon model catalysts: XPS, STM and microreactor studies, Appl. Surf. Sci. 440 (2018) 680–687, https://doi.org/10.1016/j.apsusc.2018.01.148.

[45] A. Cabot, J. Arbiol, J.R. Morante, U. Weimar, N. Bârsan, W. Göpel, Analysis of the noble metal catalytic additives introduced by impregnation of as obtained SnO₂ sol–gel nanocrystals for gas sensors, Sens. Actuator B-Chem. 70 (2000) 87–100, https://doi.org/10.1016/S0925-4005(00)00565-7.

[46] G. Kiss, V.K. Josepovits, K. Kovács, B. Ostrick, M. Fleischer, H. Meixner, F. Réti, CO sensitivity of the PtO/SnO₂ and PdO/SnO₂ layer structures: kelvin probe and XPS analysis, Thin Solid Films 436 (2003) 115–118, https://doi.org/10.1016/S0040-6090(03)00505-4.

[47] X. Yang, Y. Li, P. Zhang, R. Zhou, H. Peng, D. Liu, J. Gui, Photoinduced in situ deposition of uniform and well-dispersed PtO₂ nanoparticles on ZnO nanorods for efficient catalytic reduction of 4-nitrophenol, ACS Appl. Mater. Interfaces 10 (2018) 23154–23162, https://doi.org/10.1021/acsami.8b06815.

[48] S.K. Parayil, H.S. Kibombo, C.-M. Wu, R. Peng, T. Kindle, S. Mishra, S.P. Ahrenkiel, J. Baltrusaitis, N.M. Dimitrijevic, T. Rajh, R.T. Koodali, Synthesis-dependent oxidation state of platinum on TiO₂ and their influences on the solar simulated photocatalytic hydrogen production from water, J. Phys. Chem. C. 117 (2013) 16850–16862, https://doi.org/10.1021/jp405727k.

[49] H. Kato, K. Asakura, A. Kudo, highly efficient water splitting into H₂ and O₂ over lanthanum-doped NaTaO₃ photocatalysts with high crystallinity and surface nanostructure, J. Am. Chem. Soc. 125 (2003) 3082–3089, https://doi.org/10.1021/ja027751g.

[50] A.J. Hartmann, M. Neilson, R.N. Lamb, K. Watanabe, J.F. Scott, Ruthenium oxide and strontium ruthenate electrodes for ferroelectric thin-films capacitors, Appl. Phys. A. 70 (2000) 239–242, https://doi.org/10.1007/s003390050041.